Aalborg Universitet

Effects of modulation techniques on the input current interharmonics of Adjustable Speed Drives

Soltani, Hamid; Davari, Pooya; Zare, Firuz; Blaabjerg, Frede

Effects of modulation techniques on the input current interharmonics of Adjustable Speed Drives

Hamid Soltani, *Member, IEEE,* Pooya Davari, *Member, IEEE,* Firuz Zare, *Senior Member, IEEE,*
and Frede Blaabjerg, *Fellow, IEEE*

Abstract—Adjustable Speed Drives (ASDs) based on a three-phase front-end diode rectifier connected to a rear-end inverter may generate interharmonic distortion in the grid. The interharmonic components can create power quality problems in the distribution networks such as interference with the ripple control signals, and consequently they can hamper the normal operation of the grid. This paper presents the effect of the symmetrical regularly sampled Space Vector Modulation (SVM) and Discontinuous Pulse Width Modulation-30°lag (DPWM2) techniques, as the most popular modulation methods in the ASD applications, on the drive's input current interharmonic magnitudes. Further investigations are also devoted to the cases, where the Random Modulation (RM) technique is applied on the selected modulation strategies. The comparative results show that how different modulation techniques can influence the ASD's input current interharmonics and consequently may not be a suitable choice of modulation from interharmonics perspective. Finally, the theoretical analysis and simulation studies are validated with obtained experimental results on a 7.5 kW motor drive system.

Index Terms—Adjustable speed drive, interharmonics, harmonics, fixed-frequency modulation techniques, random modulation technique.

I. INTRODUCTION

WITH rapid advances in the power electronics technology and their continuously falling cost, the adjustable speed drives are increasingly employed in many industrial applications [1]. Energy saving and flexibility in control are considered as the main benefits of using the ASDs. However, at the same time they generate harmonic and interharmonic distortions at the grid side and deteriorate the grid power quality. In a typical standard ASD's structure, which is shown in Fig. 1, the grid AC voltages are first converted to a DC voltage via a three-phase diode rectifier followed by the DC-link filters (i.e., DC choke and DC-link capacitor). Thereafter, the rear-end inverter provides the three-phase AC output voltages required by the motor. Typically, the motor operates at a frequency other than the grid fundamental frequency. In this respect, if the drive output side harmonics leak through the inverter level and the DC-link stage, it will interact with the drive input side harmonics and consequently will give rise to the interharmonics in the grid.

Interharmonics are spectral components of voltages or currents, which are not multiple integer of the fundamental supply

H. Soltani, P. Davari and F. Blaabjerg are with the Department of Energy Technology, Aalborg University, Aalborg 9220, Denmark (e-mail: hso@et.aau.dk; pda@et.aau.dk; fbl@et.aau.dk).

F. Zare is with Power and Energy Systems, University of Queensland Brisbane St Lucia Qld 4072, Australia (e-mail: f.zare@uq.edu.au).
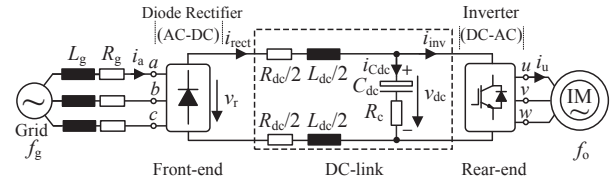
Fig. 1. Equivalent circuit of an adjustable-speed drive for system analysis with an Induction Motor (IM).

frequency [2]. The interharmonic emission is usually less significant than harmonics, but their interference with the ripple control signals has recently became a more challenging issue, which has risen especial concerns to pass limitations on their amplitudes and frequencies. Other remarkable problems caused by the interharmonic distortions are light flicker, side-band torques on the motor/generator shaft, interference with protection signals, dormant resonance excitations [3]–[7].

Interharmonic distortion issue has been subjected to many research studies and they can generally be categorized in three main sections: 1) finding the origins of interharmonics [8]–[11]; 2) accurate detection and identifications [12]–[17]; and 3) accurate modeling of the ASD [18]–[20]. However, the efforts toward finding solutions for reducing the interharmonic distortions have always been of great demand. Consequently, some active compensating strategies were introduced in [21] and [22] in order to attenuate the interharmonics distortion in the power system.

Characterization of the interharmonics in the ASDs normally needs to be considered with respect to their frequencies and amplitudes, and it needs to be analyzed during all operating conditions. Meanwhile, a precise mapping of the ASD's input current interharmonic frequencies within normal operating condition of the drive was introduced in [23], where a symmetrical regularly sampled fixed-frequency modulation technique is selected for the drive.

The interharmonic amplitude performance of the drive is significantly related to the type of modulation strategy [24], which is employed on the inverter. The SVM modulation technique is highly applied in the ASD applications due to its simple digital implementation and maximum utilization of the DC-link voltage. The next mostly used modulation strategy in the ASD is the DPWM2 technique in which the inverter pole terminals are clamped to the positive and negative DC bus each for a 60° interval within one fundamental period of the output frequency. Having a less effective switching frequency and consequently higher efficiency by applying
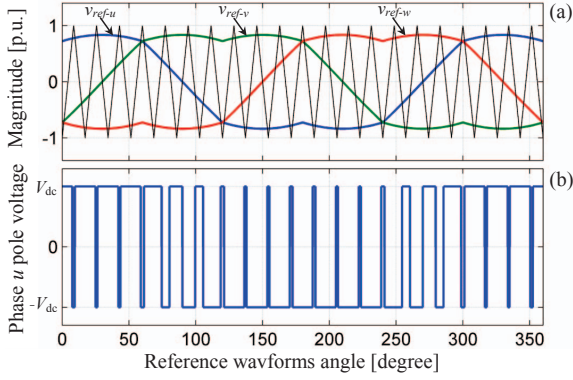
Fig. 2. The rear-end inverter SVM modulation process, (a) Three-phase reference waveforms and the carrier, (b) Inverter pole voltage in phase u.

Fig. 3. The rear-end inverter DPWM2 modulation process, (a) Three-phase reference waveforms and the carrier, (b) Inverter pole voltage in phase u.

the DPWM2 techniques has made them a popular choice of modulation in the industrial applications. Recently, applying the Random Modulation (RM) techniques along with the SVM and DPWM2 modulation strategies has also gained an increasing interest to reduce the acoustic noises in the motors. Thus, the drive interharmonic performance can be subjected to more investigations with respect to the employed modulation strategies.

Notably, the presence of many effective real-world factors have made it complicated to precisely address the interharmonics amplitude evaluation. The converter non-linearities, grid back-ground distortions and the drive passive components degradation are considered as the major factors affecting the drive input current interharmonic amplitudes. However, a comprehensive analysis performed at the same practical condition will provide an acceptable result to make a comparison, when different modulation strategies are applied.

The main aim in this paper is to carefully analyze the effects of the most popular modulation strategies (i.e., SVM, DPWM2 and RM) on the ASDs' input current interharmonics amplitude. In this respect, a step-by-step analysis has been introduced at three different stages of the ASD; the inverter level, the DC-link stage and the rectifier level. It elaborates a process through which it is shown how the DPWM2 modulation technique and its derivatives may generate higher levels of interharmonic currents compared to the SVM modulation strategy in the ASD applications.

The paper is structured as follows: first the harmonics transfer at the inverter level is fully addressed, where the effect of the SVM and DPWM2 modulation techniques are assessed with respect to the DC-link inverter-side current oscillations in Section II. Then, the ASD's passive filter role on the oscillation magnification from the DC-link inverter side to the rectifier side is presented in Section III. Afterwards in Section IV, the ASD's input current interharmonics are analyzed in terms of the selected modulation strategies. Section V briefly describes the required consideration for practical implementation. In Section VI, comparative evaluations address the results obtained for the SVM and DPWM2 techniques. Particular emphasis is also given to the drive input current interhamonics, when the RM technique is compared with the selected fixed-frequency modulation techniques. The
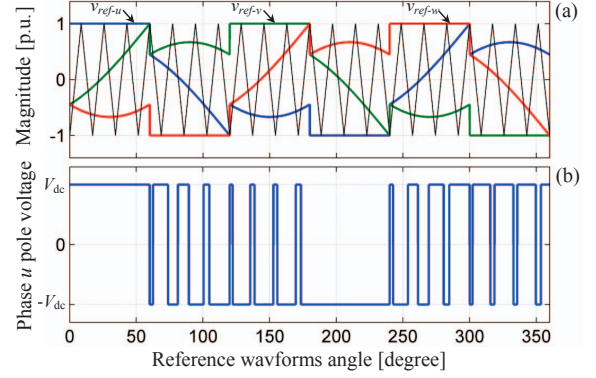
theoretical analysis and simulation studies are validated with experimental results performed on a 7.5 kW ASD.

II. DC-LINK INVERTER SIDE OSCILLATIONS CAUSED BY OUTPUT CURRENTS

The space vector modulation scheme is currently one of the most commonly used modulation strategy in the ASD systems. Fig. 2 illustrates the typical SVM modulation process with the corresponding pulsating voltage waveform in the phase a. By implementing this approach, the interactions between the inverter output phases can be recognized, and consequently it can optimize the load harmonic components. In the motor drive applications in which the Power Factor (PF) is normally around 0.86, the discontinuous pulse width modulation technique-30°lag (DPWM2) is also considered as a suitable choice of interest. In this approach, the inverter pole terminals will be locked to the positive and negative terminals of the DC link each for 60°period, as it is shown in Fig. 3, and there is no switching operation at the peaks of the load currents. As a result, a less effective switching frequency can be achieved along with having lower switching losses.

Implementing the PWM method on the rear-end inverter, as depicted in Figs. 2 and 3, typically produces the pulsating output voltages v_x ($x = u, v, w$), which are not periodic-switching waveforms, and a double Fourier integral approach is needed to find the harmonic components of the output voltages. The general form of this approach is shown in (1) with a DC value, the baseband harmonics along with the harmonics distributed around the carrier harmonics [25],

$$
\begin{aligned}
v_x(t) = \frac{A_{00}}{2} &+ \sum_{n=1}^{\infty} \left[A_{0n} \cos(n[\omega_o t - p\tfrac{2\pi}{3}]) \right. \\
&\left. + B_{0n} \sin(n[\omega_o t - p\tfrac{2\pi}{3}]) \right] \\
&+ \sum_{m=1}^{\infty} \sum_{n=-\infty}^{\infty} \left[A_{mn} \cos(m\omega_c t + n[\omega_o t - p\tfrac{2\pi}{3}]) \right. \\
&\left. + B_{mn} \sin(m\omega_c t + n[\omega_o t - p\tfrac{2\pi}{3}]) \right]
\end{aligned}
\tag{1}
$$

with m and n indicating the carrier index and the baseband index variables, respectively. The fundamental and carrier angular frequencies are also presented as ω_o and ω_c. The parameter p is 0, 1 and -1 with respect to the output phases u, v and w. The harmonic coefficients A_{mn} and B_{mn}
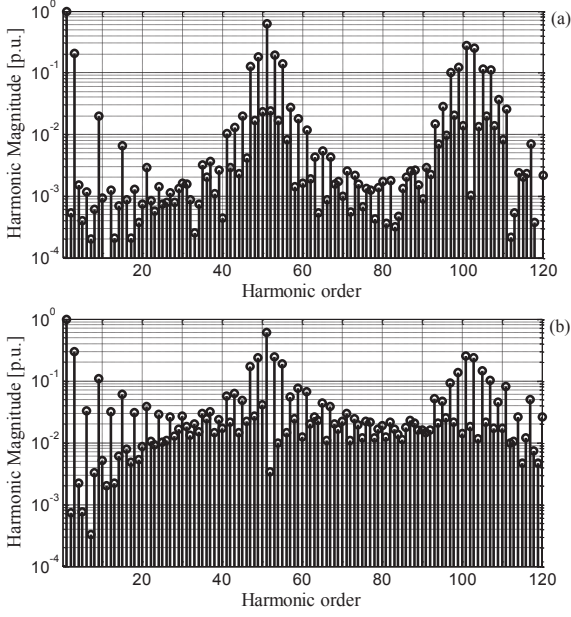
Fig. 4. Theoretical harmonic spectrum of the inverter pole voltage in phase u with the modulation index $M = 0.8$ and pulse ratio $\omega_c/\omega_o = 51$. (a) By applying the symmetrical regularly-sampled SVM modulation strategy, (b) By applying the symmetrical regularly-sampled DPWM2 modulation strategy.
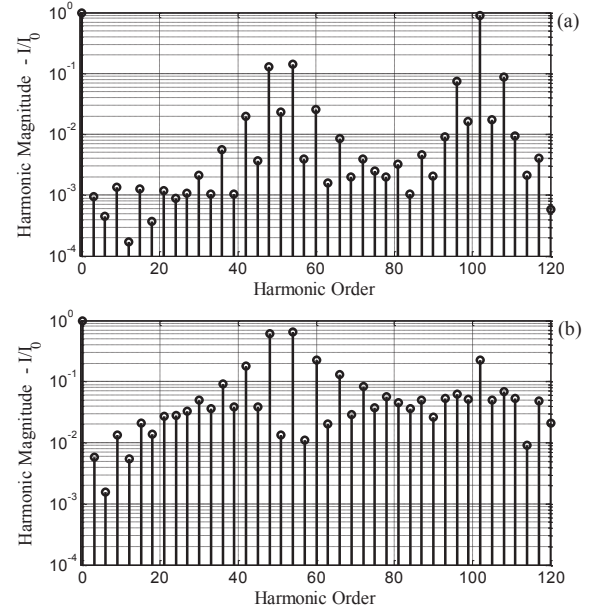

Fig. 5. Theoretical harmonic spectrum of the DC-link inverter-side current with the modulation index $M = 0.8$ and pulse ratio $\omega_c/\omega_o = 51$. (a) By applying the symmetrical regularly-sampled SVM modulation strategy, (b) By applying the symmetrical regularly-sampled DPWM2 modulation strategy.

corresponding with the double-edge symmetrical regularly sampled SVM and DPWM2 modulation techniques can be found in Appendix. It should be noted that by using the symmetrical regularly sampled modulation scheme for the SVM and DPWM2 techniques, the reference waveform is sampled and kept constant during each carrier interval, and then, is compared with the triangle carrier waveform. Fig. 4(a) and (b) illustrates the harmonic spectrum of the inverter pole voltage, when the SVM and DPWM2 modulation techniques have been applied on the inverter, respectively. The modulation index is $M = 0.8$, and a pulse ratio of $\omega_c/\omega_o = 51$ has been considered with the fundamental output frequency $f_o = 40$ Hz. The hth harmonic component is also defined in terms of m and n, and it is given as

$$h = m(\frac{\omega_c}{\omega_o}) + n \qquad (2)$$

According to Fig. 4, it can be observed that applying the DPWM2 modulation method will result in higher amplitude voltage harmonic components at the poles of the inverter compared to the SVM modulation technique.

As the main focus of this analysis is at the grid side, thus the Induction Motor (IM) model has been considered as a three-phase balanced R-L load for which the frequency domain representation of the three-phase output current $I_x(\omega)$ ($x = u, v, w$) can be extended as follows,

$$\begin{bmatrix} I_u(\omega) \\ I_v(\omega) \\ I_w(\omega) \end{bmatrix} = \frac{V_{dc}}{3Z(\omega)} \begin{bmatrix} 2 & -1 & -1 \\ -1 & 2 & -1 \\ -1 & -1 & 2 \end{bmatrix} \begin{bmatrix} S_u(\omega) \\ S_v(\omega) \\ S_w(\omega) \end{bmatrix} \qquad (3)$$

with V_{dc} and $Z(\omega)$ representing the DC value of the DC-link voltage and the frequency domain equivalent phase impedance

of the motor, respectively. $S_u(\omega)$, $S_v(\omega)$, and $S_w(\omega)$ are also the inverter switching functions and can be defined as

$$S_x(\omega) = \frac{V_x(\omega)}{V_{dc}} , \qquad x \in \{u, v, w\} \qquad (4)$$

Assuming that the inverter does not dissipate or generate power, under balanced load condition, the DC-link inverter-side current in the frequency domain $I_{inv}(\omega)$ can be obtained by summing the convolution integrals as

$$I_{inv}(\omega) = \sum_{x \in \{u, v, w\}} S_x(\omega) \otimes I_x(\omega) \qquad (5)$$

Fig. 5(a) and (b) shows the DC-link inverter side current spectra with respect to applying the symmetrical regularly-sampled SVM and DPWM2 modulation techniques on the inverter, obtained by substituting (17) and (18) (presented in the Appendix) into (3)–(5). The operating condition parameters have been considered as those used for plotting Fig. 4. It is worth to mention that with the adopted modulation strategy, the DC-link inverter-side current oscillation frequencies f_{dc}^h can be obtained as [23]

$$f_{dc}^h = 3 \cdot k \cdot f_o , \qquad k = 1, 2, 3, ... \qquad (6)$$

Based on Fig. 5(a) and (b), it is evident that applying the DPWM2 modulation strategy can give rise to a higher-amplitude DC-link current oscillations at low frequencies compared with those of the SVM modulation technique. This issue may affect the ASD's input current interharmonic amplitudes, when implementing the SVM and DPWM2 techniques on the inverter, and it will be discussed in the following sections. Moreover in the above-mentioned analysis, the DC-link voltage has been considered as a constant quantity. However in the ASD applications, the DC-link voltage usually contains several
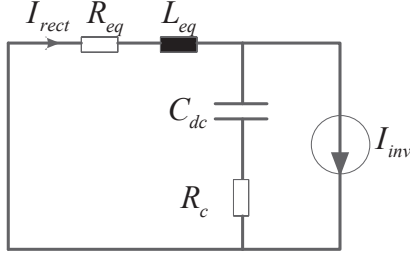
Fig. 6. DC-link equivalent circuit for motor drive.

TABLE I
Simulation and Experimental Parameter Values.

Symbol	Parameter	Value
$v_{a,b,c}$	Grid phase voltage	230 V_{rms}
f_g	Grid frequency	50 Hz
L_{dc}, R_{dc}	DC link inductor & resistor	2.5 mH, 120 mΩ
C_{dc}, R_c	DC Link Capacitor & Resistor	500 μF & 170 mΩ
v_{LL}	Induction motor rated voltage	400 V_{rms}
P_{IM}	Induction motor rated power	7.5 kW

harmonic components with the dominant one located at the frequency of $6f_g$ (f_g representing the grid voltage fundamental frequency). The effects of the DC-link voltage fluctuations will be implicitly considered in Sections III and IV.

III. PASSIVE FILTER EFFECTS ON THE DC-LINK OSCILLATIONS

The DC-link oscillations generated by the inverter operation are divided at the DC link in accordance to $i_{inv} = i_{rect} - i_{Cdc}$, where i_{rect} and i_{Cdc} are the currents flowing out of the rectifier DC terminal and through the DC-link capacitor. The DC-link equivalent circuit shown in Fig. 6 represents the current transfer from the inverter DC side to the rectifier DC side. The equivalent DC-link inductance L_{eq} and damping resistance R_{eq} are generally defined as [6]

$$L_{eq} = L_{dc} + 2L_g \quad (7)$$

$$R_{eq} = R_{dc} + 2(R_g + r_d) + \frac{3}{\pi}\omega_g L_g \quad (8)$$

with ω_g, L_g, and R_g representing the grid voltage angular frequency and the grid impedance, respectively. The diode dynamic resistance is also notated as r_d. The last term in (8) accounts for the voltage drop caused by diode commutations.

The DC-link current oscillation amplification, when passing from the inverter side to the rectifier side can then be determined by a Resonance Factor (RF), which is given as

$$RF = \frac{I_{rect}}{I_{inv}} = \left| \frac{Z_C}{Z_C + Z_L} \right| \quad (9)$$

with $Z_C = R_c + 1/(j\omega C_{dc})$, and $Z_L = R_{eq} + j\omega L_{eq}$.

The blue line in Fig. 7 shows the resonance factor of the employed ASD, whose parameters are listed in Table I. In drawing this plot, the grid side inductor L_g and the resistor R_g have been neglected, and the diode resistor value is r_d= 27 mΩ. As it can be observed, the DC-link low-frequency
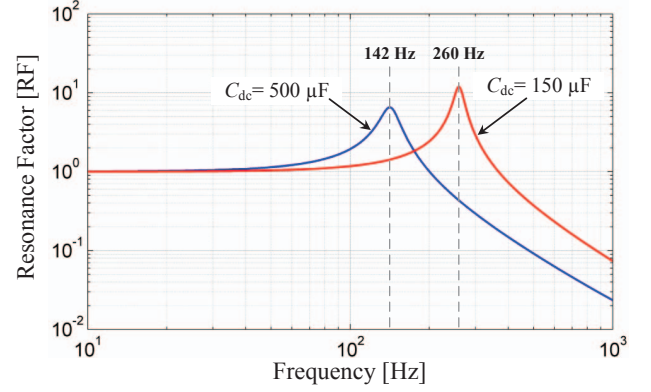
Fig. 7. DC-link Resonance Factors (RFs) obtained by using L_{eq}= 2.5 mH (with L_g= 0), R_{eq}= 174 mΩ (with R_g= 0 and r_d= 27 mΩ), and R_c= 170 mΩ for both DC-link capacitors.

(below 50 Hz) oscillations will not change in magnitude, when they pass from the inverter side to the rectifier side. Whereas, the high-frequency oscillations will be significantly attenuated at the DC link. Moreover, the presence of the DC-link oscillations inherited from the output side at the resonance area normally results in the most significant interharmonics.

The red line in Fig. 7 illustrates the resonance factor, when the DC-link capacitor size has been reduced to C_{dc} = 150 μF with the DC-link resistor value R_c=170 mΩ. In this condition, the resonance peak will be pushed to higher frequency (i.e., from 142 Hz to 260 Hz). This issue on one hand will increase the low pass area imposed by the DC-link resonance factor defined in (9), and more oscillations –coming from the output side– are allowed to leak to the grid side. However, the output side oscillations magnification depends on their frequency values. On the other hand, lowering the DC-link capacitor size will also push the resonance frequency of the drive's input impedance to higher frequencies, and it consequently may increase the amplitude of the input side harmonics, which are located at the resonance frequency. In this respect, the harmonics coming from the output side can be influenced by the input side harmonics.

IV. INTERHARMONICS GENERATION AT THE GRID SIDE

The DC-link rectifier-side current oscillations, caused by the inverter switching operation, will then be multiplied by the well-known six-pulse diode rectifier switching functions $\{S_a(t), S_b(t), S_c(t)\}$, given in (10)–(12)

$$S_a(t) = 2\sqrt{3}/\pi[\cos(\omega_g t) - 1/5\,\cos(5\omega_g t) \\ + 1/7\,\cos(7\omega_g t) - 1/11\,\cos(11\omega_g t) + ...] \quad (10)$$

$$S_b(t) = S_a(t - T/3) \quad (11)$$

$$S_c(t) = S_a(t + T/3) \quad (12)$$

with T denoting the grid voltage fundamental period.

The modulation between the DC-link harmonics, caused by inverter operation, and the rectifier switching functions will give rise to the input current interharmonic frequencies, which can be obtained as

$$f_{ih} = \left| [6 \cdot (\alpha - 1) \pm 1] \cdot f_g \pm f_{dc}^h \right| \quad \alpha = 1,\ 2,\ 3,... \quad (13)$$
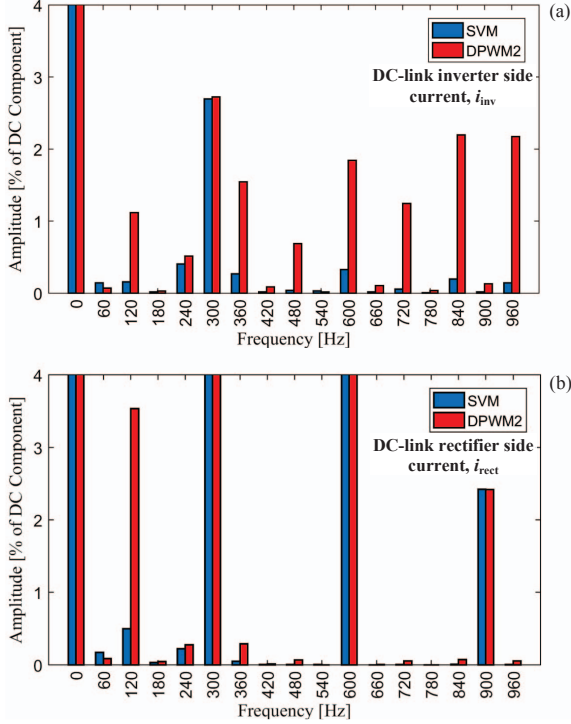
Fig. 8. Simulated drive (a) DC-link inverter side current i_{inv} harmonics, (b) DC-link rectifier side current i_{rect} harmonics, at the output frequency f_o= 40 Hz, pulse ratio ω_c/ω_o= 51, a load torque T_L= 40 Nm, and by applying the SVM and the DPWM2 modulation techniques.

Fig. 9. Simulated drive input current i_a spectra at the output frequency f_o= 40 Hz, pulse ratio ω_c/ω_o= 51, and a load torque T_L= 40 Nm with applying SVM modulation technique: (a) Harmonics and interharmonics, and (b) Output frequency versus interharmonic frequencies predicted from (13).

Fig. 10. Simulated drive input current i_a spectra at the output frequency f_o= 40 Hz, pulse ratio ω_c/ω_o= 51, and a load torque T_L= 40 Nm with applying DPWM2 modulation technique: (a) Harmonics and interharmonics, and (b) Output frequency versus interharmonic frequencies predicted from (13).

To evaluate the ASD input current interharmonics with respect to the selected modulation strategies, the drive system shown in Fig. 1 has been simulated in PLECS using those parameters listed in Table I. Fig. 8(a) and (b) shows the ASD DC-link inverter side and rectifier side currents harmonics, when it operates at the output frequency f_o= 40 Hz, the pulse ratio ω_c/ω_o= 51, and the load torque is T_L= 40 Nm. In this figure, those components with the frequency of $3kf_o(k = 1, 2, 3, ...)$ have been transferred from the inverter output side, and those harmonics located at the frequency of $6nf_g(n = 1, 2, 3, ...)$ are connected to the input side harmonics. The remaining components have been generated as a result of the interactions between the above-mentioned two groups. Based on Fig. 8(a), higher-amplitude oscillations (coming from the output side) will be generated at the DC-link inverter side current i_{inv}, by applying the DPWM2 modulation technique. The DC-link inverter side current harmonics will then be affected by the DC-link resonance factor, when they transfer to the rectifier side (see Fig. 8(b)). It is observed that the high-frequency oscillations have been significantly reduced at the DC-link rectifier side current, and it also inherits higher-amplitude harmonics (of the output side) by using the DPWM2 strategy compared to the SVM technique. Fig. 9 shows the ASD input current i_a spectra, when the SVM modulation technique is implemented on the inverter. The interharmonic frequency locations, plotted in Fig. 9(b), are obtained by substituting the DC-link oscillations of (6) into (13), with respect to the selected output frequency and the pulse ratio.

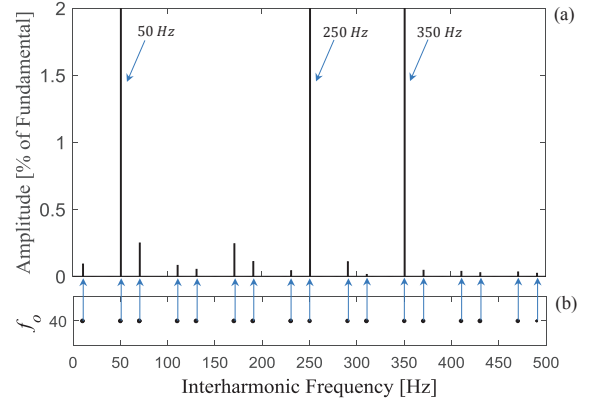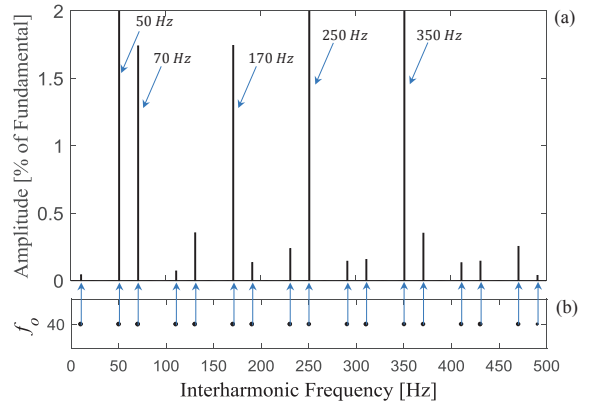Fig. 10 shows the ASD input current i_a spectra using the DPWM2 modulation technique, and at the same condition as performed for the SVM modulation case. It can be observed from Fig. 10 that applying the DPWM2 modulation technique results in higher amplitude interharmonic components in the input current compared with the SVM modulation technique. This can be validated from Fig. 8, where the DPWM2 modulation technique resulted in higher amplitude DC-link oscillations compared to the SVM strategy. This phenomenon is more significant at the interharmonic frequencies of 70 Hz and 170 Hz, which are basically generated by the 3rd order oscillation of the output frequency f_o at the DC-link stage. Moreover, referring to Fig. 9 and Fig. 10 shows that the oscillations with higher frequencies at the DC link are significantly attenuated as a result of the DC-link resonance factor, which leads to the presence of the main interharmonic components at lower frequencies.

Further assessments of the input current interharmonics have been performed by decreasing the DC-link capacitor size from C_{dc} = 500 μF used in the previous case to C_{dc} = 150 μF. Fig. 11 illustrates the harmonic spectra of the drive input current with respect to the SVM and DPWM2
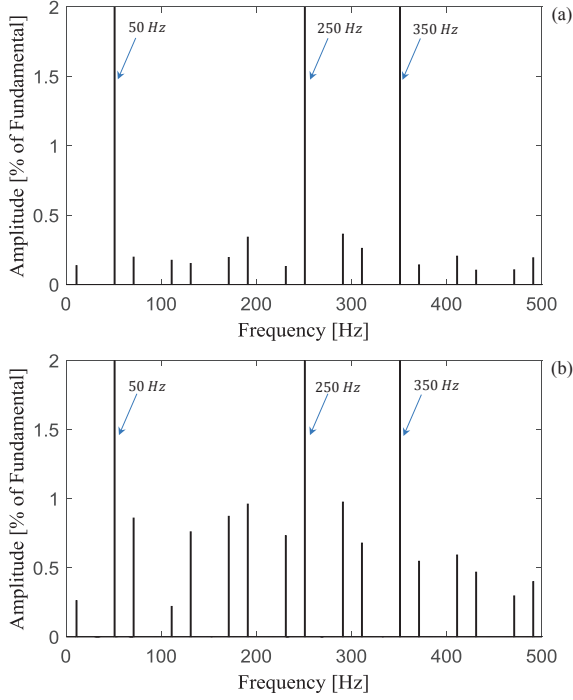
Fig. 11. Simulated drive input current i_a spectra with the DC-link capacitor C_{dc}= 150 μF, the output frequency f_o= 40 Hz, pulse ratio ω_c/ω_o= 51, and a load torque T_L= 40 Nm: (a) By applying the SVM modulation technique, (b) By applying the DPWM2 modulation technique.

modulation techniques. As it was expected from the analysis presented in Section III, it is obvious that employing smaller DC-link capacitor will highlight the role of higher order DC-link harmonics (e.g., with the frequency of 240 and 360 Hz in this case in addition to 120 Hz in the previous case) coming from the output side, and it may give rise to higher amplitude interharmonics. Meanwhile, as the DPWM2 modulation strategy can create higher amplitude harmonics (of the output frequency) in the DC-link inverter side current compared to the SVM modulation technique (see Fig. 5), it will eventually result in higher amplitude input current interharmonics.

Practically, the interharmonics amplitude analyses are influenced by many different real-world issues, and a very precise model of the investigated plant is needed to demonstrate the accuracy of the results. Especially knowing that the converter non-linearities (e.g., dead-time, turn-on voltage drop, and etc),

grid back-ground distortions, and the drive passive filter degradation may directly affect the drive input current interharmonic amplitudes. As a result, further analysis on the effect of the selected modulation techniques (i.e., SVM and DPWM2) is needed to be performed at the same practical condition. It is also worth to note that in the experimental condition, the presence of other effective factors such as a slightly load current imbalance and even the motor shaft eccentricity may give rise to the input current interharmonic components other than those created within the normal operation of the ASD.

V. Hardware Setup and Practical Implementation

A. Hardware Setup

The accuracy of the theoretical analysis was examined by a set of experiments. An experimental setup was used based on the drive system shown in Fig. 12(a), with the parameter values listed in Table I. Fig. 12(b) shows the employed experimental setup using an inverter rated at 7.5 kW. Moreover, a Chroma three-phase grid simulator was used to remove the potential grid background distortion, unbalanced voltages, and voltage fluctuations. The induction motor is controlled with a constant Voltage-to-Frequency (V/F) strategy using the 7.5 kW inverter.

B. Measurement and Analysis Method

According to IEC 61000-4-7 [26], a Discrete Fourier Transform (DFT) performed over a Rectangular time Window (RW) of exactly ten cycles for 50 Hz system or exactly twelve cycles for 60 Hz systems, corresponding to a time window width (T_w) of 200 ms is recommended for harmonic and interharmonic grouping measurement. However, employing a DFT instrument does not preclude the application of other analysis principles like wavelet analysis. There are different grouping methods but in this analysis, the harmonic and interharmonic subgrouping strategy is considered. In this respect, Harmonic Subgroup (HSG) of amplitude $C^2_{n-200-ms}$ is defined as

$$C^2_{n-200-ms} = \sum_{k=-1}^{1} C^2_{10n+k} \tag{14}$$

where C_i represents the rms value of the DFT output, shown in Fig. 13. Interharmonic Subgroup (ISG) of amplitude $C^2_{n+0.5-200-ms}$ is also defined as

$$C^2_{n+0.5-200-ms} = \sum_{k=2}^{8} C^2_{10n+k} \tag{15}$$
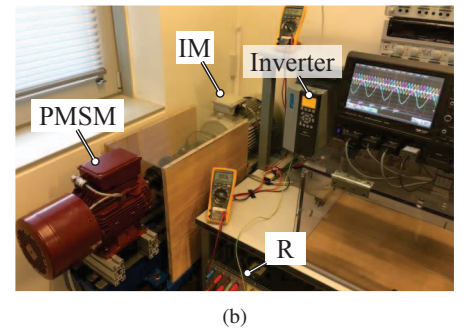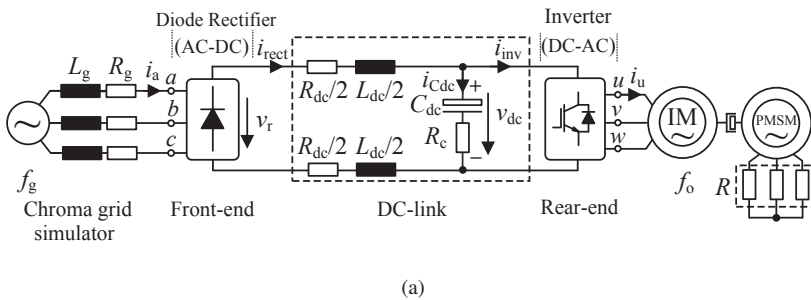

(a)

(b)

Fig. 12. Practical implementation of the ASD system, (a) Schematic of the implemented setup with an IM coupled with a Permanent Magnet Synchronous Machine (PMSM) as a load, (b) Photograph of the hardware setup.
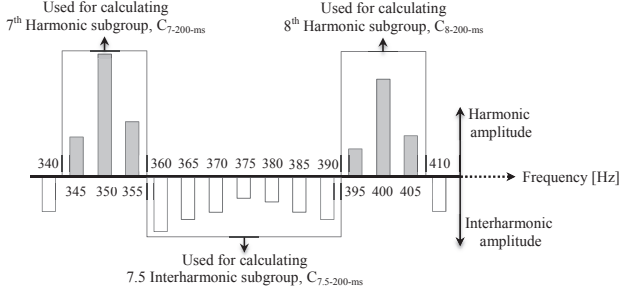
Fig. 13. Harmonics and interharmonics grouping based on IEC 61000-4-7 [26], [27].
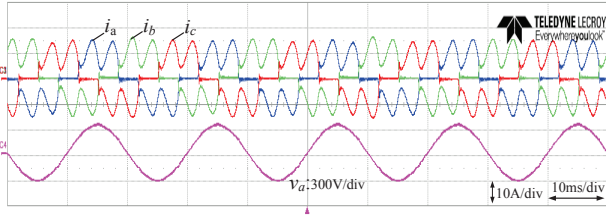

Fig. 14. The experimental three-phase drive input currents $i_{a,b,c}$ waveforms (10 A/div), and the input phase voltage v_a waveform (300 V/div) at the output frequency $f_o = 40$ Hz and the load torque $T_L = 34$ Nm.

As for the grouping results presented in the following section, in order to provide further smoothed values, an average over 15 contiguous time windows (3-s intervals) is applied. Thus the grouping values are obtained based on

$$C_{n+0.5-3-s}^2 = \frac{1}{15} \sum_{i=1}^{15} C_{i,n+0.5-200-ms}^2 \qquad (16)$$

It is worthwhile to mention that, the interharmonics detection and measurements usually suffer from the spectral leakage phenomenon and the picket fence effect, mainly due to the error in synchronizing the fundamental frequency and harmonics, and also due to the measurement of those interharmonics non-synchronized with DFT bins. In our investigation a high accuracy DFT (with a 3-second Hanning window) [27] has been implemented for showing the drive input current frequency spectrum in the next section. With this choice of windowing, an approximately 0.33 Hz frequency resolution was obtained, and the leakage problem was minimized.

VI. LABORATORY TEST RESULTS

In this section, the most common modulation techniques in ASDs application (i.e., SVM, DPWM2, SVM-RM, and DPWM2-RM) are comprehensively evaluated experimentally in terms of the drive input current interharmonic components. Fig. 14 shows the experimental ASD three-phase input current waveforms and the input phase voltage waveform, when a SVM modulation technique has been used for the inverter operation. The induction motor is also set to run at the output frequency $f_o = 40$ Hz with a load torque value of 34 Nm.

Fig. 15(a) and (b) shows the drive input current i_a frequency spectrum with respect to the applied SVM and DPWM2 modulation techniques. The motor was operating at the output frequency $f_o = 40$ Hz, with a load torque $T_L = 34$ Nm, and the
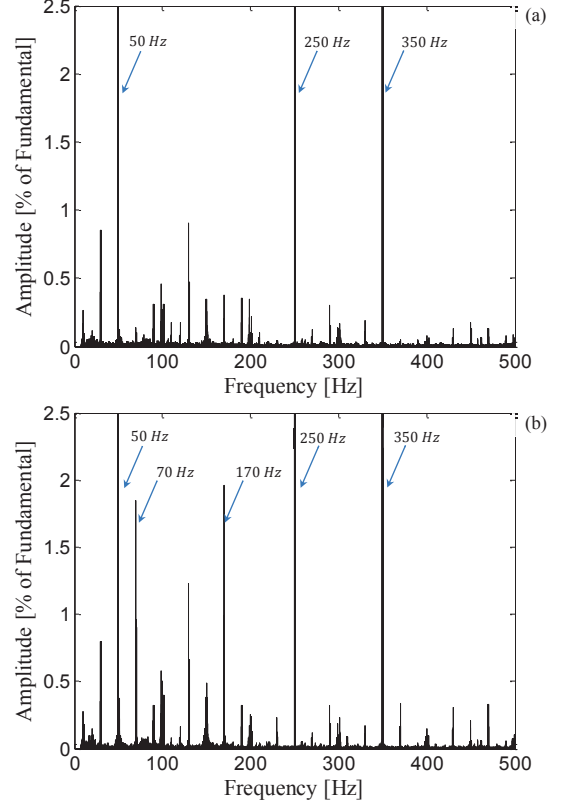

Fig. 15. Experimental drive input current i_a interharmonics at the output frequency $f_o = 40$ Hz, load torque value $T_L = 34$ Nm, and switching frequency $f_{sw} = 5$ kHz: (a) By applying the SVM modulation technique, (b) By applying the DPWM2 modulation technique.

switching frequency was set to 5 kHz. As it can be observed from Fig. 15(a), at the selected operating condition, applying the SVM modulation technique gives rise to the low-amplitude input current interharmonics (below 1% of the fundamental component). While at the same operating condition, using the DPWM2 strategy can lead to the interharmonics with higher amplitude, as shown in Fig. 15(b). Evidently, the interharmonic components appearing at 70 and 170 Hz have been significantly increased in the DPWM2 case compared with the SVM case. However, a rather unified increase can also be observed in the drive input current interharmonics, when the DPWM2 is chosen as the modulation strategy.

The examination of the drive input current i_a interharmonics was next performed, when the motor was operating at the output frequency $f_o = 36$ Hz, load torque $T_L = 32$ Nm, and at the switching frequency of 3 kHz. Notably, a lower switching frequency is intentionally chosen compared with the previous case to also investigate the significance of the drive switching frequency on the interharmonics amplitude.

Fig. 16(a) and (b) shows the associated frequency spectrum of the drive input current i_a, when the SVM and DPWM2 modulation techniques are applied on the drive. Like the previous case, it can be seen that applying the DPWM2 modulation strategy, shown in Fig. 16(b), can lead to the input current interharmonics with much higher amplitude compared with the SVM modulation strategy, shown in Fig. 16(a). Meanwhile, the interharmonic components appearing at 58 and
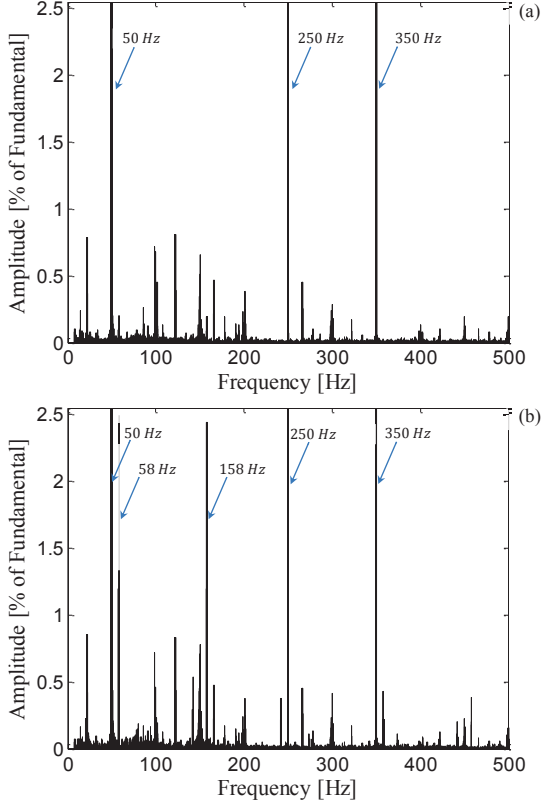
Fig. 16. Experimental drive input current i_a interharmonics at the output frequency f_o= 36 Hz, load torque value T_L= 32 Nm, and switching frequency f_{sw}= 3 kHz: (a) By applying the SVM modulation technique, (b) By applying the DPWM2 modulation technique.

Fig. 17. Experimental drive input current i_a interharmonic grouping values with applying SVM, SVM with RM, DPWM2, and DPWM2 with RM modulation techniques, when the drive is operating at the output frequency f_o = 40 Hz and a load torque T_L = 34 Nm: (a) The inverter switching frequency is f_{sw}= 3 kHz, (b) The inverter switching frequency is f_{sw}= 5 kHz.

158 Hz witness the most significant change in amplitude, when the DPWM2 strategy is applied instead of the SVM modulation technique. The significant increase in the interharmonic amplitudes, where they reach up to 2.5% of the fundamental frequency, by applying the DPWM2 modulation technique in this case will gain more importance knowing that there are ongoing discussions to put tough limitations in respect to the interharmonic amplitudes.

As it was already mentioned in Section IV, in real-life systems, the ASDs normally suffer to some extent from slightly motor current imbalance. The consequence of this issue can be observed in the experimental results presented in Figs. 15 and 16, where the dominant interharmonic components with the frequencies $2f_o \pm f_g$ (e.g., at 80±50 Hz shown in Fig. 15, and 72±50 Hz shown in Fig. 16) caused by the motor current imbalance will be added to those interharmonic components generated within the normal operating conditions of the ASD.

Further investigation of the drive input current interharmonics was performed with respect to the most common modulation strategies (i.e., SVM, SVM with RM, DPWM2, and DPWM2 with RM) applied in the ASDs, where the grouping measurement technique (presented in (16)) evaluates the drive performance. Fig. 17 shows the comparison results, when the motor was operating at the output frequency f_o = 40 Hz with a load torque T_L = 34 Nm. The interharmonic group amplitudes in respect to the selected modulation strategies are compared in Fig. 17(a), where a switching frequency f_{sw} of
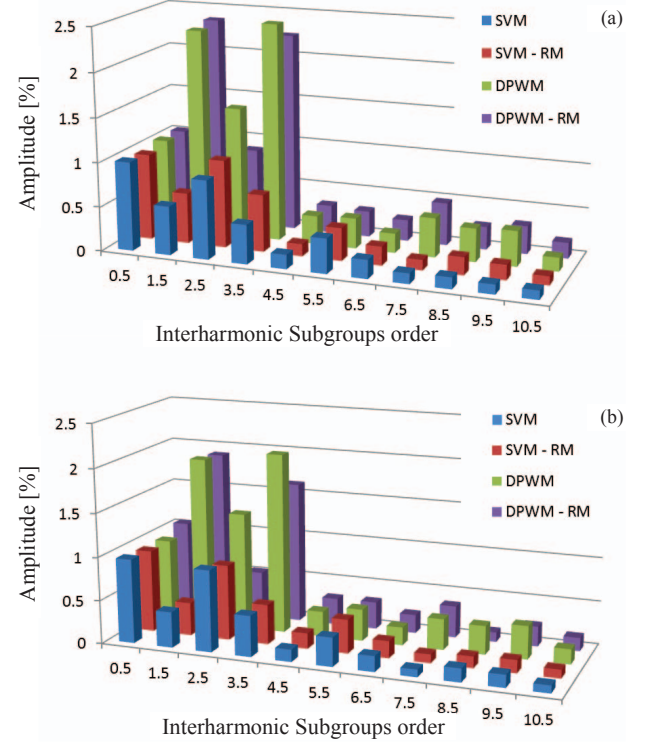
3 kHz is chosen in the drive. It should be noted that the interharmonic groups order 0.5, 1.5, 2.5,..., and 10.5 presented in Fig. 17 are corresponding to the frequency ranges [10–40], [60–90], [110–140],..., and [510–540] Hz, respectively. The interharmonic group amplitudes are also normalized with respect to the rms value of the fundamental frequency.

As it can be seen from Fig. 17(a), the interharmonic group amplitudes with applying the DPWM2 and DPWM2-RM modulation strategies are sensibly higher compared with the SVM and SVM-RM modulation techniques. Meanwhile, the ISG of order 1.5 and 3.5 are recognized as the worst interharmonic groups mainly due to the presence of the high-amplitude interharmonic components accommodated at 70 and 170 Hz in this operating condition. Moreover, particular attention to evaluate the drive input current interharmonics by applying the RM modulation strategies shows a slight difference compared with the associated fixed-frequency technique in respect to the interharmonic group amplitudes. Notably, the frequency variation around the switching frequency for the RM technique is not significant, therefore the captured energy through the grouping method is not changed considerably.

Fig. 17(b) shows the grouping evaluation results of the input current i_a interharmonics, when the drive operates at the switching frequency of 5 kHz. Like the results presented in Fig. 17(a) related to the switching frequency of 3 kHz, the ISG of order 1.5 and 3.5 are the worst interharmonic groups at this operating condition. A comparison of the results obtained at the switching frequencies of 3 and 5 kHz, shown in Fig. 17,
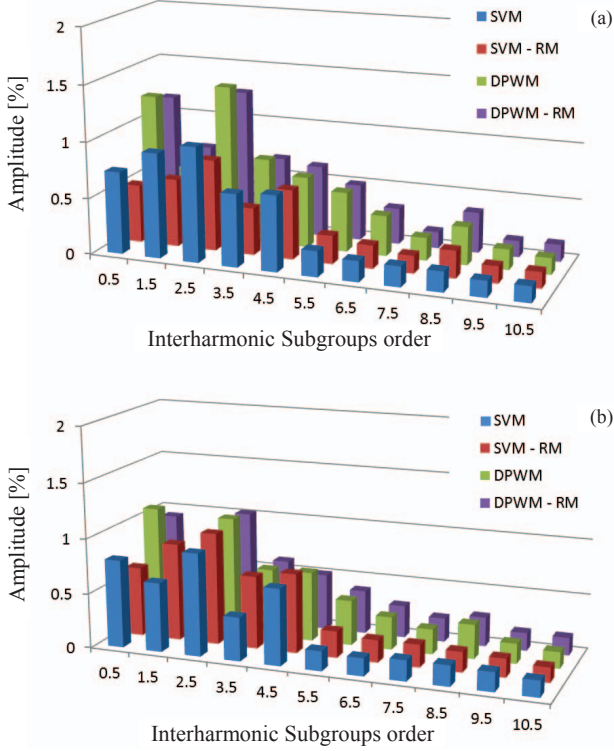
Fig. 18. Experimental drive input current i_a interharmonic grouping values with applying SVM, SVM with RM, DPWM2, and DPWM2 with RM modulation techniques, when the drive is operating at the output frequency f_o = 30 Hz and a load torque T_L = 28 Nm: (a) The inverter switching frequency is f_{sw} = 3 kHz, (b) The inverter switching frequency is f_{sw} = 5 kHz.

shows that the interharmonic group amplitudes will be higher, when lower switching frequency is selected on the drive. This issue will gain more importance in the high-power motor drive applications with very low switching frequency.

Finally, the evaluation of the drive input current i_a interharmonics is performed at the output frequency f_o = 30 Hz and a load torque T_L = 28 Nm, and the corresponding results are shown in Fig. 18. The results obtained at the switching frequency of 3 kHz, shown in Fig. 18(a), imply that applying the DPWM2 and DPWM2 with RM modulation techniques are associated with the most significant input current interharmonics in the ASD. In this operating condition, the worst interharmonic group amplitudes belong to the ISG of order 0.5 and 2.5, where the higher-amplitude 3rd order DC-link oscillation of the output frequency f_o by applying the DPWM technique is expected to generate distinguishable input current interharmonic components mainly at 40 and 140 Hz. Fig. 18(b) shows the comparative results of interharmonic grouping amplitudes at the drive switching frequency of 5 kHz, where it indicates better performance of the drive by applying the SVM modulation technique.

Generally, an appropriate selection of the drive's switching frequency depends on the ASD system power level. Operating at higher switching frequencies increases the switching losses and reduces the system efficiency. Moreover, increasing the switching frequency can elevate the EMI issues. In this work, a switching frequency f_{sw} = 5 kHz has been first selected, which it is a suitable value for the investigated range of power.

Thereafter, another switching frequency (i.e., f_{sw} = 3 kHz) has been chosen basically due to the fact that from interharmonic perspective, more concerns may be raised, when the drive operates at lower switching frequencies.

To sum up, the modulation techniques are usually evaluated based on the appropriate objectives and operating condition required in different applications. For instance, the DPWM2 technique has less effective switching frequency and it improves the efficiency of the system, which makes it popular to be implemented further in the ASD applications. But at the same time, employing this technique may affect the harmonic and interharmonic distortions. In the same way, implementing different RM methods (random frequency, random pulse position, random zero vector injection, or their combination) can lead to different performances with respect to the interharmonic emissions. In this respect, the results presented in this paper emphasize the role of the selected modulation techniques on the ASD's interharmonics, which can be utilized in further trade-off for selecting the desired modulation strategy.

VII. CONCLUSION

In this paper, the input current interharmonics generated by the adjustable speed drive have been comprehensively evaluated with respect to the most common modulation strategies (i.e., SVM, SVM with RM, DPWM2, and DPWM2 with RM). The effects of the SVM and DPWM2 modulation techniques on the associated DC-link oscillations are first analyzed followed by introducing the role of the ASD passive filters on the DC-link oscillations magnification. Then, the input current interharmonic amplitudes have been investigated in terms of the SVM and DPWM2 modulation methods. Although applying the DPWM2 modulation strategy is gaining more attention recently due to less effective switching frequency and consequently lower losses, according to this investigation it is not a suitable choice of modulation from interharmonics point of view compared to using the SVM modulation strategy. It is also shown that at the same operating condition of the ASD, lower switching frequency may give rise to higher-amplitude interharmonic components, especially when the DPWM2 modulation technique is chosen on the inverter. Particular emphasis was also dedicated to the drive input current interharmonic grouping amplitudes with applying the RM modulation techniques, where it was shown that small improvement can be achieved at some operating conditions of the ASD. The results obtained by PLECS simulation and several experimental tests demonstrate accuracy of the analytical calculations.

VIII. APPENDIX

The harmonic coefficients A_{mn} and B_{mn} in (1) can be evaluated for each $60°$ sextant, using the double Fourier integral. The closed form theoretical harmonic solution for the double-edge symmetrical regularly sampled SVM and DPWM2 modulation techniques are given in (17) and (18) respectively (at the bottom of next page), where $q = m + n(\omega_o/\omega_c)$. The coefficients in (17) and (18) contains $J_y(z)$, which represents the Bessel functions of the first kind of the order y and argument z.

REFERENCES

[1] P. Davari, Y. Yang, F. Zare, and F. Blaabjerg, "A multi-pulse pattern modulation scheme for harmonic mitigation in three-phase multi-motor drives," *IEEE J. Emerg. Sel. Top. Power Electron.*, vol. 4, no. 1, pp. 174–185, Mar. 2016.

[2] IEEE Interharmonic Task Force, "Interharmonics: theory and modeling," *IEEE Trans. Power Del.*, vol. 22, no. 4, pp. 2335–2348, Oct. 2007.

[3] D. Gallo, C. Landi, R. Langella, and A. Testa, "IEC flickermeter response to interharmonic pollution," presented at the 11th Int. Conf. Harmonics and Quality of Power, Lake Placid, NY, 2004, pp. 489–494.

[4] M. Hernes and B. Gustavsen, "Simulation of shaft vibrations due to interaction between turbine-generator train and power electronic converters at the visund oil platform," in *Proc. IEEE Power Convers. Conf. (PCC)*, 2002, pp. 1381–1386.

[5] F. Wang and M. Bollen, "Measurement of 182 Hz interharmonics and their impact on relay operation," in *Proc. IEEE-ICHQP Conf.*, 2000, pp. 55–60.

[6] D. Basic, "Input current interharmonics of variable-speed drives due to motor current imbalance," *IEEE Trans. Power Del.*, vol. 25, no. 4, pp. 2797–2806, Oct. 2010.

[7] H. Soltani, F. Blaabjerg, F. Zare, and P. C. Loh, "Effects of passive components on the input current interharmonics of adjustable-speed drives," *IEEE J. Emerg. Sel. Top. Power Electron.*, vol. 4, no. 1, pp. 152–161, Mar. 2016.

[8] R. Yacamini, "Power system harmonics. Part 4: Interharmonics," *Power Eng. J.*, vol. 10, no. 4, pp. 185–193, Aug. 1996.

[9] E. W. Gunther, "Interharmonics in power systems," in *Proc. IEEE Power Eng. Soc. Summer Meeting*, 2001, pp. 813–817.

[10] D. Gallo, R. Langella, and A. Testa, "On the processing of harmonics and interharmonics in electrical power systems," in *Proc. IEEE Power Eng. Soc. Winter Meeting*, 2000, pp. 1581–1586.

[11] M. Rifai, T. H. Ortmeyer, and W. J. McQuillan, "Evaluation of current interharmonics from AC drives," *IEEE Trans. Power Del.*, vol. 15, no. 3, pp. 1094–1098, Jul. 2000.

[12] G. Chang, C. Chen, Y. Liu, and M. Wu, "Measuring power system harmonics and interharmonics by an improved fast Fourier transform-based algorithm," *IET Gener. Transm. Distrib.*, vol. 2, no. 2, pp. 193–201, Mar. 2008.

[13] C.-I. Chen and Y.-C. Chen, "Comparative study of harmonic and inter-harmonic estimation methods for stationary and time-varying signals," *IEEE Trans. Ind. Electron.*, vol. 61, no. 1, pp. 397–404, Jan. 2014.

[14] F. Cupertino, E. Lavopa, P. Zanchetta, M. Sumner, and L. Salvatore, "Running DFT-based PLL algorithm for frequency, phase, and amplitude tracking in aircraft electrical systems," *IEEE Trans. Ind. Electron.*, vol. 58, no. 3, pp. 1027–1035, Mar. 2011.

[15] I. Sadinezhad and V. G. Agelidis, "Frequency adaptive least-squares-Kalman technique for real-time voltage envelope and flicker estimation," *IEEE Trans. Ind. Electron.*, vol. 59, no. 8, pp. 3330–3341, Aug. 2012.

[16] C.-I. Chen and G. W. Chang, "An efficient Prony-based solution procedure for tracking of power system voltage variations," *IEEE Trans. Ind. Electron.*, vol. 60, no. 7, pp. 2681–2688, Jul. 2013.

[17] H. C. Lin, "Power harmonics and interharmonics measurement using recursive group-harmonic power minimizing algorithm," *IEEE Trans. Ind. Electron.*, vol. 59, no. 2, pp. 1184–1193, Feb. 2012.

[18] W. Xu, H. W. Dommel, M. B. Hughes, G. W. Chang, and L. Tan, "Modelling of adjustable speed drives for power system harmonic analysis," *IEEE Trans. Power Del.*, vol. 14, no. 2, pp. 595–601, Apr. 1999.

[19] R. Carbone, F. De Rosa, R. Langella, and A. Testa, "A new approach for the computation of harmonics and interharmonics produced by line-commutated AC/DC/AC converters," *IEEE Trans. Power Del.*, vol. 20, no. 3, pp. 2227–2234, Jul. 2005.

[20] G. W. Chang and S. K. Chen, "An analytical approach for characterizing harmonic and interharmonic currents generated by VSI-fed adjustable speed drives," *IEEE Trans. Power Del.*, vol. 20, no. 4, pp. 2585–2593, Oct. 2005.

[21] E. Delaney and R. Morrison, "Minimisation of interharmonic currents from a current source AC drive by means of a selective DC side active filter," *IEEE Trans. Power Del.*, vol. 10, no. 3, pp. 1584–1590, Jul. 1995.

[22] L. Feola, R. Langella, A. Testa, L. Herman, and I. Papic, "On the use of unbalance definition to control compensators for arc furnaces," in *IEEE International Workshop on Applied Measurements for Power Systems*, 2013, pp. 29–34.

[23] H. Soltani, P. Davari, F. Zare, P. C. Loh, and F. Blaabjerg, "Characterization of Input Current Interharmonics in Adjustable Speed Drives," *IEEE Trans. Power Electron.*, vol. PP, no. 99, pp. 1–1, Dec. 2016.

[24] Danfoss: Facts Worth Knowing about Frequency Converters. Nordborg, Denmark: Danfoss, 2008.

[25] D. G. Holmes and T. A. Lipo, *Pulse width modulation for power converters: principles and practice*. John Wiley & Sons, 2003, vol. 18.

[26] *Electromagnetic compatibility (EMC) – Part 4-7: Testing and Measurement TechniquesGeneral Guide on Harmonics and Interharmonics Measurements and Instrumentation, for Power Supply Systems and Equipment Connected Thereto*, IEC Std. 61000-4-7.

[27] A. Testa, D. Gallo, and R. Langella, "On the processing of harmonics and interharmonics: using Hanning window in standard framework," *IEEE Trans. Power Del.*, vol. 19, no. 1, pp. 28–34, Jan. 2004.

$$A_{mn} + jB_{mn} = \frac{8V_{dc}}{q\pi^2}\begin{pmatrix} \frac{\pi}{6}\sin([q+n]\frac{\pi}{2})(J_n(q\frac{3\pi}{4}M) + 2\cos(n\frac{\pi}{6})J_n(q\frac{\sqrt{3}\pi}{4}M)) \\ +\frac{1}{n}\sin(q\frac{\pi}{2})\cos(n\frac{\pi}{2})\sin(n\frac{\pi}{6})(J_0(q\frac{3\pi}{4}M) - J_0(q\frac{\sqrt{3}\pi}{4}M))\,|n \neq 0 \\ +\sum_{\substack{k=1 \\ k\neq -n}}^{\infty}[\frac{1}{n+k}\sin([q+k]\frac{\pi}{2})\cos([n+k]\frac{\pi}{2})\sin([n+k]\frac{\pi}{6}) \\ (J_k(q\frac{3\pi}{4}M) + 2\cos([2n+3k]\frac{\pi}{6})J_k(q\frac{\sqrt{3}\pi}{4}M))] \\ +\sum_{\substack{k=1 \\ k\neq n}}^{\infty}[\frac{1}{n-k}\sin([q+k]\frac{\pi}{2})\cos([n-k]\frac{\pi}{2})\sin([n-k]\frac{\pi}{6}) \\ (J_k(q\frac{3\pi}{4}M) + 2\cos([2n-3k]\frac{\pi}{6})J_k(q\frac{\sqrt{3}\pi}{4}M))] \end{pmatrix} \tag{17}$$

$$A_{mn} + jB_{mn} = \frac{2V_{dc}}{q\pi^2}\begin{pmatrix} \frac{4\pi}{3}\cos(n\frac{\pi}{6})\sin([q+n]\frac{\pi}{2})\cos(q\frac{\pi}{2})J_n(q\frac{\sqrt{3}\pi}{2}M) \\ +\frac{1}{n}\sin(q\pi)\sin(n\frac{\pi}{3})(1 - J_0(q\frac{\sqrt{3}\pi}{2}M))\,|n \neq 0 \\ +\frac{j}{n}\sin(q\pi)(1-\cos(n\frac{\pi}{3}))(2\cos(2n\frac{\pi}{3})J_0(q\frac{\sqrt{3}\pi}{2}M)+1)\,|n \neq 0 \\ +\sum_{\substack{k=1 \\ k\neq -n}}^{\infty}[\frac{2}{n+k}J_k(q\frac{\sqrt{3}\pi}{2}M)[\sin([2q+k]\frac{\pi}{2})\cos([4n+5k]\frac{\pi}{6}) \\ +\sin(k\frac{\pi}{2})\cos([2n+k]\frac{\pi}{6})][\sin([n+k]\frac{\pi}{3})+j(1-\cos([n+k]\frac{\pi}{3}))]] \\ +\sum_{\substack{k=1 \\ k\neq n}}^{\infty}[\frac{2}{n-k}J_k(q\frac{\sqrt{3}\pi}{2}M)[\sin([2q+k]\frac{\pi}{2})\cos([4n-5k]\frac{\pi}{6}) \\ +\sin(k\frac{\pi}{2})\cos([2n-k]\frac{\pi}{6})][\sin([n-k]\frac{\pi}{3})+j(1-\cos([n-k]\frac{\pi}{3}))]] \end{pmatrix} \tag{18}$$